Forecasting for Future CMB Searches for Primordial Magnetic Fields

THE UNIVERSITY OF
MELBOURNE

Dylan Sutton
Supervised by Dr. Christian Reichardt

27th May 2016

Abstract

Contents

1 Introduction

The standard model for cosmology, ΛCDM cosmology postulates that the Universe is homogeneous, isotropic and contains both cold dark matter (CDM) and dark energy (Λ). ΛCDM is very successful at describing the Universe. However there remain many outstanding problems in the model that beg for a solution. One such problem is the mysterious origin of the large-scale magnetic fields permeating the cosmos. Detections of Faraday rotation, synchrotron emissions and Zeeman splitting in distant galaxies and throughout intracluster media reveal weak magnetic fields, on the order of microgauss coherent over the scale of megaparsecs. Though it is easy to amplify existing magnetic fields, for instance with magnetohydrodynamics and galactic dynamos, there is no clear method for producing a seed magnetic field from zero initial conditions.

Primordial magnetic fields (PMFs) are conjectured as seed magnetic fields produced in the early Universe. These weak seed fields - of order nanoguass - may be produced sometime before recombination and could be taken up by galactic dynamos to become the weak magnetic fields we see today. So far PMFs remain undetected, but the next generations of Cosmic Microwave Background (CMB) experiments beginning over the next decade offer the chance to indirectly observe their effects. Stage-3 CMB experiments such as SPT-3G, Advanced ACTPol and the Simons array will come online in 2016 and 2017. The specifications of the stage-3 experiments are already decided but stage-4 experiments have yet to be designed. It is therefore important to know how sensitive stage-3 experiments will be to the faint traces of PMFs as well as how to best design a stage-4 experiment such that we have the best chance of detecting them. The aim of this thesis is to forecast the upper-limits on PMF detections for stage-3 and stage-4-like CMB experiments.

In this chapter I will begin by discussing the nature of the large-scale magnetic fields and the physics behind their amplification due to galactic dynamos in section 2.1. In section 2.2 I will discuss recent advances in constraining the PMF strength. Next, in section 2.3 I will give a quick review on CMB observables, polarisation and power spectra - which are instrumental in the study of PMFs. Finally in section 2.4 I will discuss the basic experimental design of stage-3 CMB experiments as well as preliminary figures on stage-4 experiments.

1.1 Observational Evidence for Large Scale Magnetic Fields

Galaxy clusters are the largest gravitationally bound objects in the Universe. Each contains thousands of galaxies. Weak microgauss magnetic fields, coherent over mega parsec scales have been observed permeating these clusters and their resident galaxies. Observational evidence of these magnetic fields come in the form of Zeeman splitting, synchrotron emission and Faraday rotation.

1.1.1 Zeeman Splitting

In the presence of magnetic fields, electron energy levels in molecules and atoms split based on the angular momentum of the electron with respect to the orientation of the magnetic field, this effect is known as Zeeman splitting. Zeeman splitting can be detected in spectral lines, allowing us to probe magnetic fields in distant sources. Splitting of the Hydrogen 21cm line and the OH 18cm line are common probes of magnetic fields in our own galaxy. Looking further out, Zeeman splitting has also been used to measure the magnetic fields within dense gas clouds around nearby galaxies, with strengths in the order of 0.5-18mG [Robishaw et al., 2008], however these regions are not representative of the large-scale magnetic fields threading the cosmos which are of order microgauss, as measured through synchrotron emissions and Faraday rotation. For the time being Zeeman splitting reaches its limits beyond the neighbouring galaxies, with no constraints on the magnetic fields threading the intracluster medium.

1.1.2 Synchrotron Emissions

As electrons and ions spiral around magnetic fields in galaxies and the intracluster medium they emit synchrotron radiation with energies proportional to the strength of the magnetic field and the velocity of the ions [Giovannini, 2004].

The emissivity of synchrotron radiation is given by:

$$j(B_\perp, \nu) \propto n_0 B_\perp^{(1+\alpha)/2} \nu^{(1-\alpha)/2} \tag{1}$$

where ν is the frequency of the electron's circular motion, $B_\perp$ is the magnetic field component perpendicular to the line of sight and n_0 is the normalised electron density, given by $n_e dE = n_0 E^{-\alpha} dE$ where E is the energy of the electron and α is the spectral index, the value for which varies from galaxy to galaxy. [Buczilowski and Beck, 1991] measured synchrotron emissions to calculate the magnetic field strength of nearby galaxies and found the average magnetic field strength to be $9 \pm 3\mu G$ [Buczilowski and Beck, 1991].

1.1.3 Faraday Rotation

As photons travel through a magnetised plasma they undergo Faraday Rotation. Magnetised plasmas such as the intracluster medium exhibit different refractive indices for left and right circularly polarised light. Hence, as linearly polarised light propagates through the plasma, its plane of polarisation is rotated by some some angle, ψ, given by:

$$\psi = RM\lambda^2 \tag{2}$$

where λ is the wavelength of the photon and RM is the rotation measure, given by:

$$RM = \frac{e^3}{2\pi^2 \epsilon_0 m^2 c^3} \int_0^d n_e(s) B_\parallel(s) ds \tag{3}$$

where the prefactors are: e, the electron charge, ϵ_0, the vacuum permittivity, m, the mass of the electron and c, the speed of light in a vacuum. By (2) and (3) the angle of rotation depends on the electron density, n_e in the plasma, the component of the magnetic field parallel to the direction of propagation of the photon, $B_\parallel$ and the photon's wavelength, λ.

Measurements of Faraday rotation within galaxy clusters have found the magnetic field strength to lie in the range of 0.2 - 3 μG [Widrow, 2002]. In additon, Faraday rotation measurements yield typical magnetic field strengths in galaxies at the level of 4 - 6 μG for spiral galaxies and 6 - 8 μG in elliptical and irregular galaxies [Widrow, 2002].

1.2   Cosmic Microwave Background Polarisation

In the last few years CMB polarisation has proven a powerful tool for studying large scale strucutre and the early Universe. If PMFs did in fact exist, then their traces ought to be found within the CMB polarisation. Section 2 contains a discussion on how PMFs affect CMB polarisation.

The CMB is the light from the Big Bang, however the CMB itself didn't form until 300,000 years after the Big Bang. At this point in time the Universe was cool enough to allow photons to decouple from baryons. This event is known as last scattering. From there on the photons were able to free stream through the cosmos. Over the intervening 13 billion years the CMB photons have been cosmologically redshifted into the microwave frequency band. The CMB is a blackbody spectrum corresponding to a temperature of 2.73K.

At the time of last scattering the Universe was composed of a hot, ionised plasma, consisting of protons and electrons. The temperature anisotropies in this plasma gave rise to the net polarisation of the CMB that we see today [Hu and White, 1997]. Electrons in the plasma are surrounded by hot and cold patches. Those that are surrounded by quadrupolar temperature anisotropies - two hotter patches either side and then two cooler patches either side on an axis perpendicular to the hotter patches produce a net polarisation through Thomson scattering.

Figure 1 shows how a net linear polarisation arises from Thomson scattering about a quadrupolar temperature anisotropy. Two photons approach the electron from perpendicular directions, one from the cool patch (shown in red) and one from the hot patch (shown in blue). The two photons scatter off the electron perpendicular to the plane of incidence for both photons. The resultant photon has a net linear polarisation oriented in the plane of incidence with an angle of polarisation proportional to the difference in temperature of the two photons.

Quadrupolar anisotropies are caused by scalar, vector or tensor perturbations. Scalar perturbations are density fluctuations. Vector perturbations result from vortices in the photon-
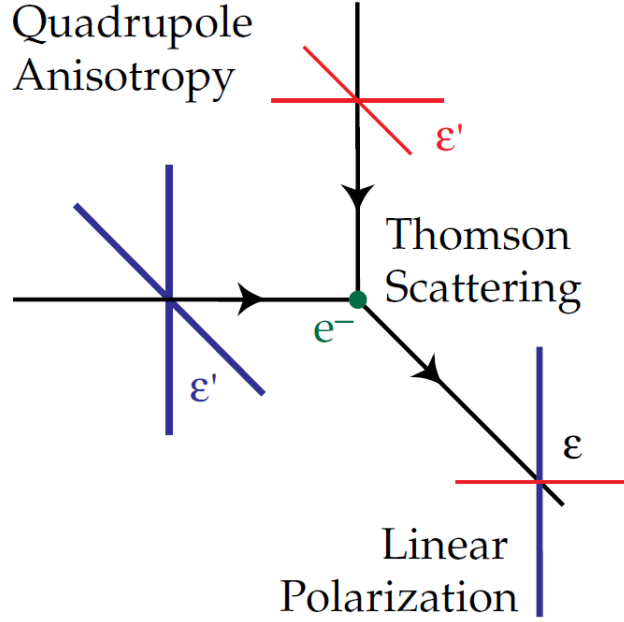
Figure 1: Thomson scattering of CMB photons in the presence of a quadrupole anisotropy. The red lines are the polarisations of a cold photon and the blue lines are the polarisations of a hot photon both incident on the same electron. The result is a net linear polarisation. Figure from [Hu and White, 1997]

electron fluid or from more exotic phenomena, such as cosmic strings and other topologcal defects. Finally a tensor perturbation would be the result of gravity waves produced during cosmic inflation.

In order to describe the effects of perturbations on CMB polarisation we introduce two polarisation modes. E-modes and B-modes. E-modes are formed from scalar perturbations. The E-modes resemble electric fields in electromagnetism in the sense that they are curl-free. The left panel in figure 2 shows the two forms of E-modes. The bottom mode has zero divergence whereas the top mode has non-zero divergence. It is clear to see that E-modes are symmetric under reflection, in other words they have even parity. B-modes on the other hand are formed from vector and tensor perturbations. As we will see in section, B-mode polarisation holds the key to indirectly detecting and constraining the magnitude of PMFs. Continuing the electromagnetism analogy a B-mode resembles a magnetic field, in the sense that it is purely a curl field. Figure 2 shows B-modes on the right panel. There are two forms, each rotating in opposite directions. B-modes are anti-symmetric under reflection - that is reflecting one gives you the other. This property illustrates their characteristic odd parity.
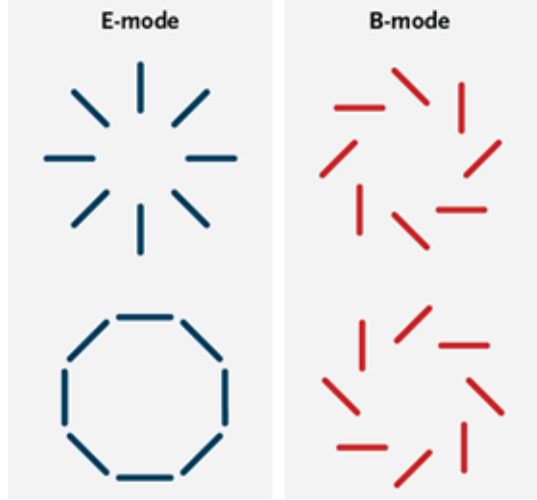
Figure 2: Representation of E-mode polarisations and B-mode polarisations. Note how E-modes are symmetric and resemble a divergent field. In contrast the B-modes appear anti-symmetric and resemble a curled field. Figure from [Krauss et al., 2010]

1.3   Future CMB experiments

This year stage-3 CMB experiments will commence operation and before the end of the next decade, stage-4 CMB experiments will have also collected their data. The next generation of CMB experiments aim to obtain tighter constraints on cosmological parameters such as the tensor-to-scalar ratio as well as map the CMB in higher detail than ever before. Though PMF detection is not the main science goal of these experiments, they will be able to tighten constraints on the primordial magnetic field strength and perhaps make a detection.

Since CMB polarisation has such a faint signal, it is essential that all CMB experiments aim to reduce their level of noise as much as possible. There are many ways to do this - making better detectors or perhaps adding more. In the case of CMB experiments one can produce better detectors by reducing the temperature of the detector. This however has diminishing returns at low temperatures since firstly, lower temperatures are progressively harder to reach and sustain the lower they are. Secondly, current CMB detectors are already well below the temperature of the incoming CMB photons, so the improvement from reducing the temperature any further is negligible.

Instead, the standard approach to lowering noise is to simply add more detectors. This works since photon detection is a Poisson process, that is only discrete numbers of photons can be detected, the rate at which they hit the detector is constant and independent of previous photon detection events and a detector can only detect a single photon at a time. For a Poisson process, the noise level scales with the number of the detectors like:

$$Noise \propto \frac{1}{\sqrt{N_{detectors}}} \tag{4}$$

so far, each stage of CMB experiments have added a factor of 10 more detectors, bringing

9

the noise level down by a factor of $\sqrt{10}$.
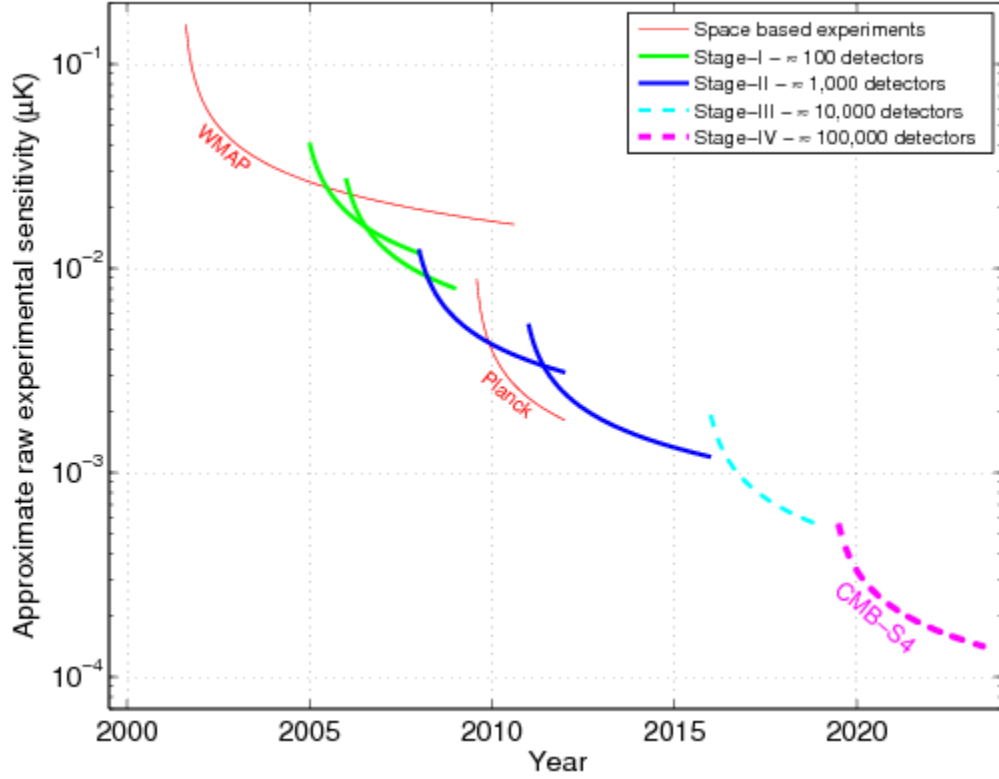
Figure 3: Plot of approximate raw experimental sensitivity of CMB experiments vs time in years. The Red lines indicate space-based experiments. Of note is PLANCK whose sensitivity falls in the middle-range of the stage-2 CMB experiments. The dotted cyan line represents the sensitivity of CMB-S3, which we expect to improve by up to an order of magnitude over Stage 2. CMB-S4 is represented by the dotted purple line, which is set to improve by a further order of magnitude over S3. Figure from [Abazajian et al., 2015]

Table 1: Properties of Present and Future CMB experiments

Experiment	Stage	N_{bolo}	Survey Area (deg^2)	Polarisation Noise (μK)
SPT-pol	2	1 536	100	20
PLANCK	Space-based	-	41 253	52
Adv-ACTpol	3	2 718	20 000	9.9
SPT-3G	3	15 234	2 500	4.8
Simons Array	3	22 764	33 000	4.8
Stage 4 Expected	4	500 000	20 000	1.4

table shows a short (and by no means comprehensive) list of current and upcoming CMB experiments and their key design features useful for detecting PMFs.

[Henderson et al., 2016] [Benson et al., 2014] [Suzuki et al., 2016] [Adam et al., 2016]. The PLANCK telescope is the only space-based experiment listed on this table. I have included it because I will use its data release in my analysis. The number of detectors has been left out since the number of detectors on ground and space-based experiment can't be directly compared. For reference PLANCK has 32 polarisation detectors on its High Frequency Instrument (HFI) and carries out full-sky observations [Lamarre et al., 2003].

2   Primordial Magnetic Field Theory

2.1   Biermann Batteries

The large-scale magnetic fields we see need to have had some initial seed field, but of course this raises the question: Where did the seed field come from? The most popular model for seed magnetic field generation from zero initial conditions is the 'Biermann battery' proposed by Biermann in 1950. Biermann batteries form in highly ionised environments such as the plasma shortly afer the Big Bang. Within the plasma, ions are drawn to regions of lower density and lower temperature. Since the the constituents of the plasma - protons and electrons - have different masses they flow at different rates resulting in a net flow of charge. If this flow of current forms a loop, then by Faraday's law of induction, a magnetic field is produced by the battery.

The magnetic field produced by the Biermann battery is described by:

$$\frac{\partial \vec{B}}{\partial t} = \nabla \times (\vec{U} \times \vec{B} - \eta \nabla \times \vec{B}) - \frac{ck_b}{e} \frac{\nabla n_e}{n_e} \times \nabla T \tag{5}$$

The final term, $\nabla n_e \times \nabla T$ is the source term describing the Biermann battery effect. In order for this term to be non-zero and hence to have a Biermann battery, gradients of the electron density and the temperature must be non-parallel.

2.2   Other Methods of PMF Generation

2.2.1   Inflation

Cosmic inflation is an attactive model for PMF generation since since it both explains how a seed magnetic field could end up coherent over megaparsec scales and provides a simple mechanism for generating a seed field from zero initial conditons. During inflation the seed field may emerge due to the absence of any ionised plasma during cosmic inflation. At this time the Universe isn't yet a good conductor. In this state the magnetic flux is not a conserved quantity and hence it's possible for a seed field to emerge spontaneously [Turner and Widrow, 1988].

In inflationary theory, the exponential growth of the scale factor is responsible for stretching quantum fluctuations into large-scale density perturbations that seed large-scale structures such as galaxies and galaxy clusters. Similarly inflation may be able to take up a PMF field that spontaneously arises in the early Universe. A small fluctuation in the magnetic flux density could be stretched out over megaparsec scales and amplified by magnetohdydrodynamics in the intervening epochs between inflation and now [Turner and Widrow, 1988].

A problem for this model is that it requires inflation to break conformal symmetry to produce this weak seed field initially. [Turner and Widrow, 1988] present one such model for confor-

mal symmetry breaking leading to PMF generation as well as provide a deeper discussion of the reasons for studying inflation as the cause of PMF formation.

2.2.2 Phase Transitions

PMFs may have also been produced by early phase transitions, such as the QCD transition or the electroweak phase transition. During a phase transition bubbles of the new phase form within the previous phase, these bubbles grow and collide until the entire Universe reaches the lower phase. These phase transitions bring on non-equilibrium processes such as leptogenesis and baryogenesis, which may be responsible for producing some weak magnetic fields. Within a phase transition, a collision between bubbles will produce turbulence leading to dynamos which will serve to spin up the magnetic fields into the strengths required to match the field strengths observed today.

2.3 Galactic Dynamos as Amplifiers

On their own, seed magnetic fields such as PMFs are too weak (of order nanoguass) to give rise to the magnetic fields we see in the cosmos today. There must be a process for amplifying the seed magnetic fields. Galactic dynamos are good candidates for seed magnetic field amplifiers. Dynamos are systems that convert kinetic energy into electromagnetic energy. Hot ionised gas rotates around the galactic centre of a galaxy. The ions drag the magnetic field lines along with them, tangling them up and increasing the magnetic flux density, and in addition the magnetic field strength. Hence galactic dynamos are able to amplify a weak seed magnetic field into a stronger magnetic field that we observe today.

2.4 Effect of PMFs on the Cosmic Microwave Background

If PMFs have a field strength 1nG then their signatures will be detectable in the CMB B-mode polarisation power spectrum. Just as extragalactic magnetic fields Farday rotate radio and X-ray signals, PMFs would induce Faraday rotation within CMB polarisation. The net effect is that a fraction of E-mode polarisation would be transformed into B-mode polarisation. The PMF power spectrum is given by:

$$P(k) = A_{PMF} k^{n_B} \tag{6}$$

Where A_{PMF} is the PMF amplitude and n_B is the PMF spectral index. Since the scale of the PMF power spectrum will depend on the age of the Universe when they first formed, the spectral index is sensitive to the mechanism that first produced PMFs.
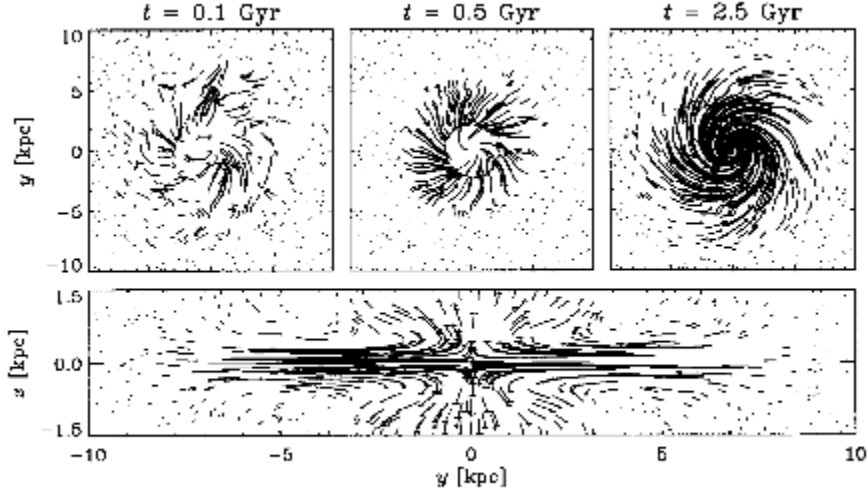
Figure 4: Spin up of magnetic fields in the presence of a galactic dynamo. In the first panel, at t = 0.1 Gyr, the seed magnetic field is picked up by a dynamo. Over the next two panels the dynamo spins up the magnetic field, increasing flux density. The bottom panel is a side-on view of the galactic dynamo at 8.1 Gyr. Figure from Beck et al., (1996) [Beck et al.,].

In order to measure the strength of PMFs we focus our attention to the amplitude, A_{PMF}. The PMF amplitude is related to B_{1Mpc}, the strength of PMFs coherent over 1 megaparsec by the following relation:

$$A_{PMF} = (\frac{B_{1Mpc}}{2.5nG})^4 \tag{7}$$

Recent work from PLANCK (2015) has constrained the primordial magnetic field strength coherent over 1 Mpc to $B_{1Mpc} < 4.4nG$ [Ade et al., 2015b]. In 2016 POLARBEAR modestly improved this constraint to $B_{1Mpc} < 3.9nG$ [Ade et al., 2015c].

2.5   Other effects of PMFs

In addition to CMB polarisation, PMFs will affect the have effects on large scale structure and Big Bang Nucleosynthesis (BBN).

2.5.1   Large Scale Structure

PMFs can indirectly shape the the structure of the cosmos. At early times a PMF can exert a Lorentz force on baryonic matter. Since baryonic matter interacts gravitationally with
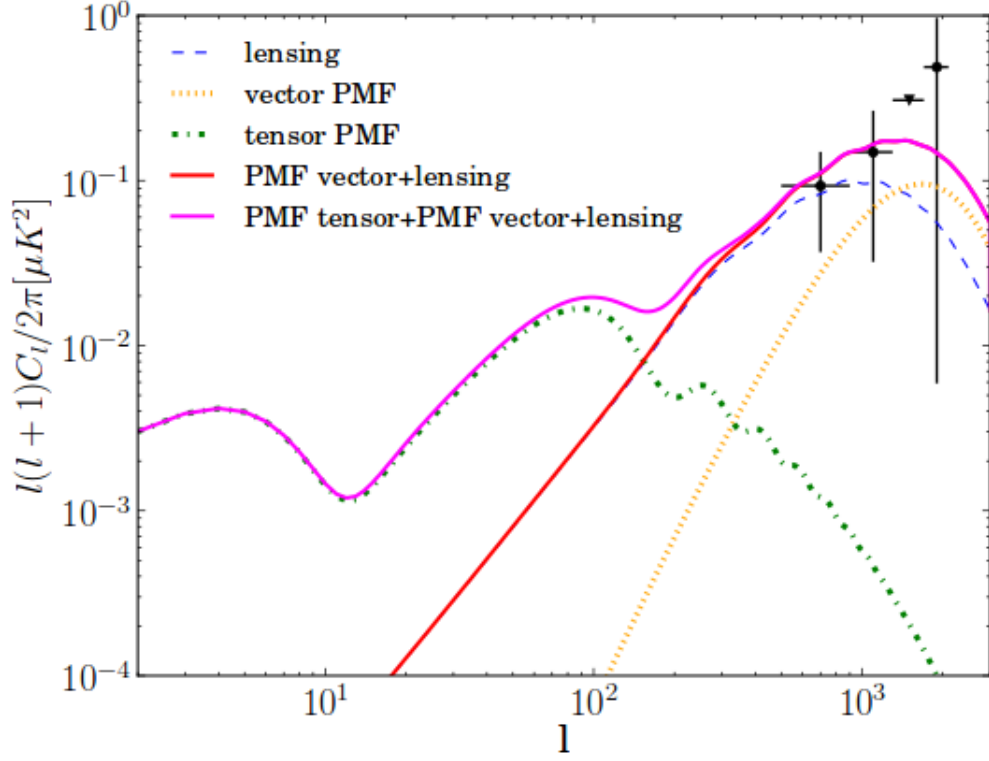
Figure 5: Plot of the CMB power spectrum. The dotted green and yellow lines show the power spectrum for vector and tensor PMFs. Vector PMFs have more power on smaller scales (larger ℓ) and tensor PMFs have more power on larger scales (smaller ℓ). The purple line shows the expected combined PMF plus lensing effects on the CMB. Compared to the blue dotted line for lensing alone, a PMF-influenced CMB power spectrum may be detectable on smaller scales than on larger scales.

dark matter, it follows that PMFs have an influence on matter distribution. This effect can be observed in the density perturbation amplitude over 8 Mpc, σ_8. One can also observe its effects by looking for changes in the matter power spectrum. figure 6 shows the impact of PMFs on the matter power spectrum for Universes with either massless or massive neutrinos.

So far, there are no constraints on the PMF amplitude from large scale structure as the interactions happen in the non-linear regime, making measurements of its effects difucult at the current time.

2.5.2 Big Bang Nucleosynthesis

If PMFs existed prior to BBN then we expect to see its signature in nuclear abundances. Primordial magnetic fields contribute to the overall energy density of the Universe and therefore vary the rate of expansion. If the rates of expansion in the Universe differ then so does
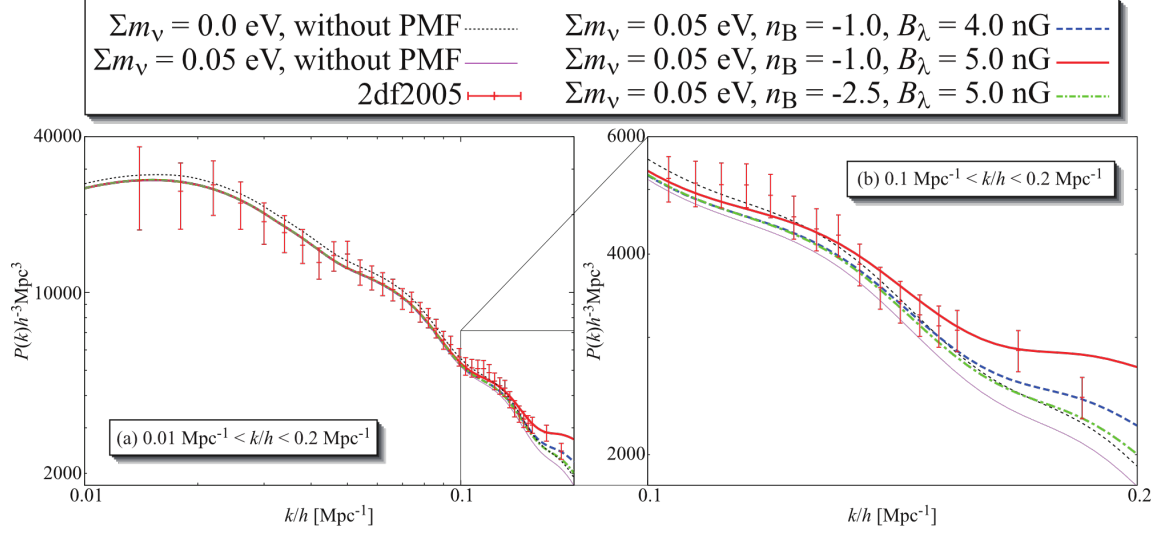
Figure 6: Plot of the matter power spectrum. Here B_λ is equal to B_{1Mpc} The left panel gives the power spectrum in the range $0.01 Mpc^{-1} < k/h < 0.2 Mpc^{-1}$. At small scales (small k/h) all models fall within the experimental error, however the Universe without massive neutrinos or PMFs has more power at these scales. The right panel gives the power spectrum in the range $0.1 Mpc^{-1} < k/h < 0.2 Mpc^{-1}$. At larger scales, the matter power spectrum is significantly affected by the presence and strength of PMFs.

the rate at which the Universe cools. If PMFs were indeed formed prior to BBN then the freeze-out times of reactions during BBN would differ from standard model values and hence so would primordial abundances of Helium and Hydrogen.

The strongest constraints from BBN have $B_{1Mpc} < 1.5~\mu G$ [Kawasaki and Kusakabe, 2012]. These constraints are far weaker than those currently given by CMB polarisation measurements.

2.6 Other Sources of Cosmic Birefringence

The rotation of E-mode polarisation to B-mode polarisation is not a phenomenon unique to PMFs. Another mechanism for this effect may be quintessence. Quintessence is an alternative explanation to the cosmological constant for the accelerating expansion of the Universe. It argues that there may exist a long-range pseudoscalar field that can very weakly couple to baryons. The interaction is described by the Chern-Simons term:

$$\mathcal{L} \propto \frac{\phi}{2M} F_{\mu\nu} \tilde{F}^{\mu\nu} \tag{8}$$

Where ϕ is the pseudoscalar field and M is the mass of the field boson. If photons couple to this field, then their polarisation will be rotated, just as they would if there were a PMF.

The rotation angle due to the pseudoscalar field is given by:

$$\alpha = \frac{1}{M} \int d\eta \dot{\phi} \tag{9}$$

Where $\dot{\phi}$ is integrated over the conformal time η

Currently we constrain the effects of cosmic birefringence with an equivalent effective PMF, however by comparing the two-point and four-point correlation functions it is possible to differentiate between effects due to PMFs and effects due to conjectured quintessence models. [Ade et al., 2015c]

3 Method

In this section I outline the method I used to forecast upper limits for PMF detection using mock stage-3 and stage-4 covariance matrices and simulated CMB power spectra. In section 3.1 I will introduce the Fisher matrix, its properties and discuss how it is useful for experimental design. In section 3.2 I will discuss how I obtained CMB power spectra and how they are used to construct the Fisher matrix. Next, in section 3.3 I will describe the properties of the mock covariances and how I processed them into a useable format. Finally in section 3.4 will bring all the pieces together and explain how to obtain a Fisher matrix, apply conditioning to secure it against numerical instabilities and apply a change of variables to recieve forecasts for the upper limits on B_{1Mpc}.

3.1 Introduction to Fisher Matrices

The Fisher matrix is a powerful tool in experimental design, allowing us to forecast the theoretical maximum precision for a planned experiment. In my research I constructed Fisher matrices for future CMB experiments and inverted them into covariance matrices over the many model parameters a CMB experiment can measure with the aim of finding the theoretical maximum precision for an experiment aiming to measure or constrain the field strength of PMFs.

The elements of the Fisher matrix are defined as:

$$\mathcal{F}_{ij} = -\left\langle \frac{\partial^2 ln\mathcal{L}}{\partial p^i \partial p^j} \right\rangle \tag{10}$$

where $\mathcal{L}$ is the likelihood and p^i, p^j are the ith and j^{th} model parameters.

If the Fisher matrix is non-singular then it can be inverted into a covariance matrix for the model parameters. This result follows from the Cramèr-Rao theorem, which states that the variance of some unbiased estimator, p is greater than or equal to the inverse of its Fisher information. The Fisher information of a model parameter is given by:

$$F = -\langle \frac{\partial^2 ln\mathcal{L}}{\partial p^2} \rangle \tag{11}$$

Since the Fisher matrix can be inverted into a covariance matrix over the model parameters, it is a powerful tool in experimental design used for forecasting the upper limits on the precision of an experiment. The Fisher matrix has a number of useful properties.

Suppose I would like to know not only how well one CMB experiment will do, but rather the whole set of CMB experiments within a generation. If I had the covariance matrices for each individual experiment the solution is simple. I can just invert each covariance matrix into a Fisher matrix and use the fact that Fisher matrices are linear under addition. Adding the

many Fisher matrices together returns a new Fisher matrix which can be inverted into a new covariance matrix with tighter constraints accounting for the net precision of all the CMB experiments. In general, if I have n Fisher matrices I can add them together and invert like so:

$$(\mathcal{F}_1 + \mathcal{F}_2 + ... + \mathcal{F}_n)^{-1} = \mathcal{F}_{1+2+...+n}^{-1} \tag{12}$$

As a corollary, the Fisher matrix can be multiplied by a scalar, which is useful when you want to know the effect of repeating your experiment or adding more instances of the same design. Furthermore, one can use this property to add priors to your design: suppose we know that one model parameter has been well-constrained in the past and our experiment isn't set to improve upon this result. We can combine the prior result with our current Fisher matrix to provide tighter constraints, like so:

$$\begin{bmatrix} F_{aa} & F_{ab} & F_{ac} \\ F_{ba} & F_{bb} & F_{bc} \\ F_{ca} & F_{cb} & F_{cc} \end{bmatrix} + \begin{bmatrix} 0 & 0 & 0 \\ 0 & 0 & 0 \\ 0 & 0 & P \end{bmatrix} \tag{13}$$

Here, I have a prior, P on a variable, c. All I need to do is add P to the corresponding diagonal term. However, if the prior is too big the Fisher matrix becomes numerically singular. This is a nuisance when dealing with large data sets and many model parameters however there are ways to combat this. I employ the second useful property of Fisher matrices, marginalisation.

If I have a Fisher matrix with more variables than we're interested in, I can just remove the rows and columns associated with the variables that I don't care about. The resultant matrix is a Fisher matrix that is valid for the remaining variables - there's no need to recalculate the Fisher matrix with fewer variables!

Returning to the case where $P \gg F_{cc}$, we can marginalise over the variable c by removing its associated rows and columns from the Fisher matrix. In this case the information lost is negligible, since the variance from our experiment was much larger than P's experiment anyway. In return, we now find we can forecast for the remaining variables.

Equation 9 defines a case where one must know the log-likelihoods over the model parameters. There are special cases where this need not be done. If the model parameters are unbiased and Gaussian distributed then the following definition for the Fisher matrix holds:

$$F_{ij} = \frac{\partial f}{\partial p^i} C^{-1} \frac{\partial f}{\partial p^j} \tag{14}$$

where f is the function that relates the model parameters to each other, C is the covariance matrix for the experimental design and p^i are the model parameters. In this thesis I will take f to be the CMB polarisation power spectrum, C_ℓ. Next, p will be the ΛCDM parameters as well as some additional parameters (see table 2) and finally C are mock covariance matrices associated with CMB-S3-like and CMB-S4-like experiments. Equation (12) then becomes:

$$F_{ij} = \frac{\partial C_\ell}{\partial p^i} C^{-1} \frac{\partial C_\ell}{\partial p^j} \tag{15}$$

3.2   The CMB Power Spectra

To begin constructing the Fisher matrix in the form given by 15, I first used CAMB to build the CMB power spectrum. ?????????????????????????????????

To call on CAMB one first needs to define parameters. A quick summary of the parameters and their central values is given in table 2. The parameters I varied were the six ΛCDM model parameters: $\Omega_b h^2$, the baryonic density. $\Omega_c h^2$, the cold dark matter density. H_0, Hubble's constant. τ, the optical depth of reionisation. τ is a measure of approximately when reionisation occurred. n_s, the scalar spectral index for the primordial power spectrum, given by $P(k) = A_s k^{n_s-1}$. A_s is the amplitude of the primordial power spectrum. In addition we also have: The running of the scalar index, n_{run}. The effective number of neutrinos, N_{eff} and the tensor-to-scalar ratio, r, which is used in constraining the effects of primordial gravity waves.

Table 2: CAMB Parameters and Values

Parameter	Value	Uncertainty	Step Size
$\Omega_b h^2$	0.02227716	0.00023	$\pm 8 \times 10^{-5}$
$\Omega_c h^2$	0.1184293	0.022	$\pm 10^{-3}$
H_0	67.86682	0.96	$\pm 8 \times 10^{-2}$
τ	0.06664549	0.019	$\pm 10^{-3}$
n_s	0.9682903	0.0062	$\pm 10^{-3}$
A_s	2.140509e-09	0.118	$\pm 9 \times 10^{-12}$
n_{run}	0.0	-	$\pm 2 \times 10^{-3}$
N_{eff}	3.03066666667	0.23	$\pm 4 \times 10^{-3}$
r	0.01	-	$\pm 8 \times 10^{-3}$

This table shows the 6 ΛCDM model parameters, as well as the running of the scalar index, the effective number of neutrinos and the tensor-to-scalar ratio. The 'Value' column shows the central value I entered into CAMB when producing the polarisation power spectrum and the 'Step Size' column indicates the magnitude of the perturbation around the central value I used for calculating the numerical derivatives. Finally, the 'Uncertianty' column gives the PLANCK best fit (2015) [Ade et al., 2015a] ΛCDM uncertainties, which were used as an upper bound for step sizes.

In order to differentiate the power spectrum as required by 15 I employ a numerical form of the derivative:

$$\frac{\partial C_\ell}{\partial p} \approx \frac{\Delta C_\ell}{\Delta p} \tag{16}$$
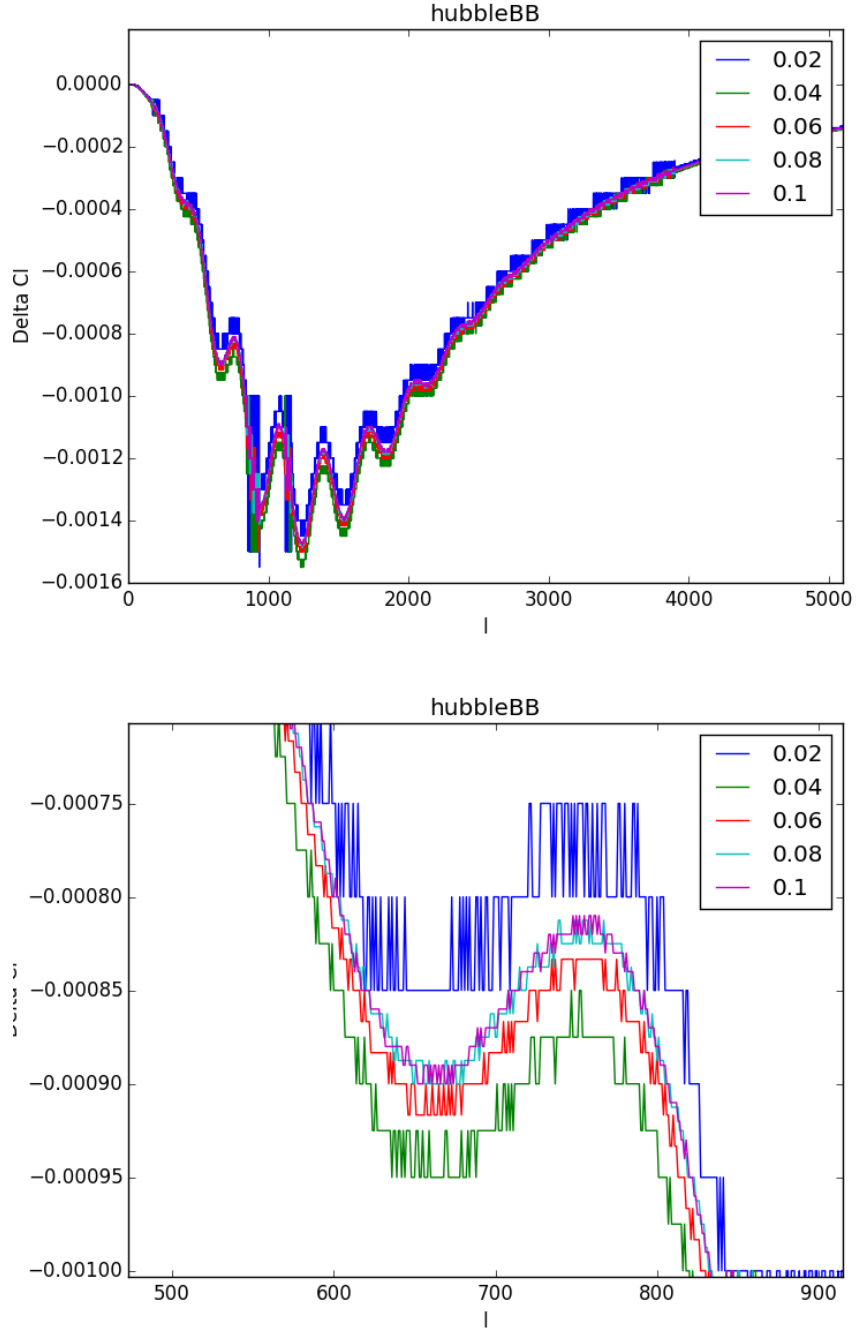
20

Figure 7: Plot of CMB BB power spectrum difference when H_0 is varied for different step sizes. Top panel: Power spectrum over the range $0 \leq \ell \leq 5000$. This plot shows that ΔC_ℓ converges within this range. Smaller step sizes show less stability, as shown by the blue and green lines. Bottom panel: A zoomed in version of the above graph, taken over $500 \leq \ell \leq 900$. The larger of the step sizes, given by the cyan and magenta lines have a lot of overlap, which indicates that the derivatives will converge on a step-size within the range 0.08 to 0.1

Where $\Delta C_\ell = C_\ell^{upper} - C_\ell^{lower}$ and $\Delta p = p^{upper} - p^{lower}$. To calculate ΔC_ℓ I call two instances of CAMB. In the first instance I add small perturbations to the central values (see table 2). The output power spectrum is called C_ℓ^{upper}. The second instance, C_ℓ^{lower} has small perturbations subtracted from the central values. Finally, Δp is equal to two times the perturbation values given in table 2.

To ensure that the derivatives are accurate the step sizes must be small, however if the step size is too small, the derivatives are subject to numerical artifacts. To choose well-conditioned step sizes I isolated each variable and generated a set of ΔC_ℓs while holding all other parameters fixed and varying the step size. To compare the step sizes I then plotted each family of ΔC_ℓ. When choosing a step size I looked for two things:

1. Convergence: As the step size approaches the best value, ΔC_ℓ will lose sensitivity to changes in step-size and the functions will converge to the same values for all ℓ.

2. Smoothness: If the step size is too small then ΔC_ℓ will oscillate significantly over a short change in ℓ. The resultant plot will look 'blocky' or have large spikes and won't resemble a well-conditioned derivative of the CMB power spectrum.

As a final sanity check on the value of the step sizes, I would like them to be less than the 2015 PLANCK best fit uncertainties (refer to table 2).

Figure 7 shows a plot of ΔC_ℓ for the BB polarisation power spectrum, varying Hubble's constant and holding all else fixed. The top panel shows the differences over $0 < \ell < 5000$. The lines all appear to be converging on the same function. The blue line, corresponding to a step size of 0.02 has significant artifacting, so by criterion one it can be ruled out. The second panel is zoomed in on the peak and trough over ℓ 700. Taking a closer look at the lines reveals that as the step size increases toward 0.1 the lines begin to converge. There isn't an ostensible difference between step sizes of 0.08 or 0.1, so the deciding factor is which one produces a better approximation of $\frac{\partial C_\ell}{\partial p}$. Smaller step sizes suit this purpose so for Hubble's constant I chose 0.08.

An interesting second case is the difference plot for the tensor-to-scalar ratio. When $\ell < 220$ the difference plot is well behaved with good convergence and few artifacts for larger step sizes. When $\ell > 220$ numerical effects begin to dominate. This occurs since CAMB isn't programmed to handle variations in the tensor-to-scalar ratio as cleanly as the more standard parameters. This will likely be addressed in the future, once the value for r is found and its effects can be properly studied. For now, one can easily remedy this adding a low pass filter, keeping $\ell < 220$ and discarding the rest, since we expect that r is only significant at low ℓ. However this might be a drastic response. Since the effects of r are small, it is safe to ignore these artifacts without any significant change in the result. Indeed, perturbing around my chosen step size in r yields negligble variations in the Fisher matrix.

In addition to the CAMB power spectra I also PMF templates which were generated using the method from [Ade et al., 2015c] and [Gluscevic et al., 2009]. These templates are the PMF
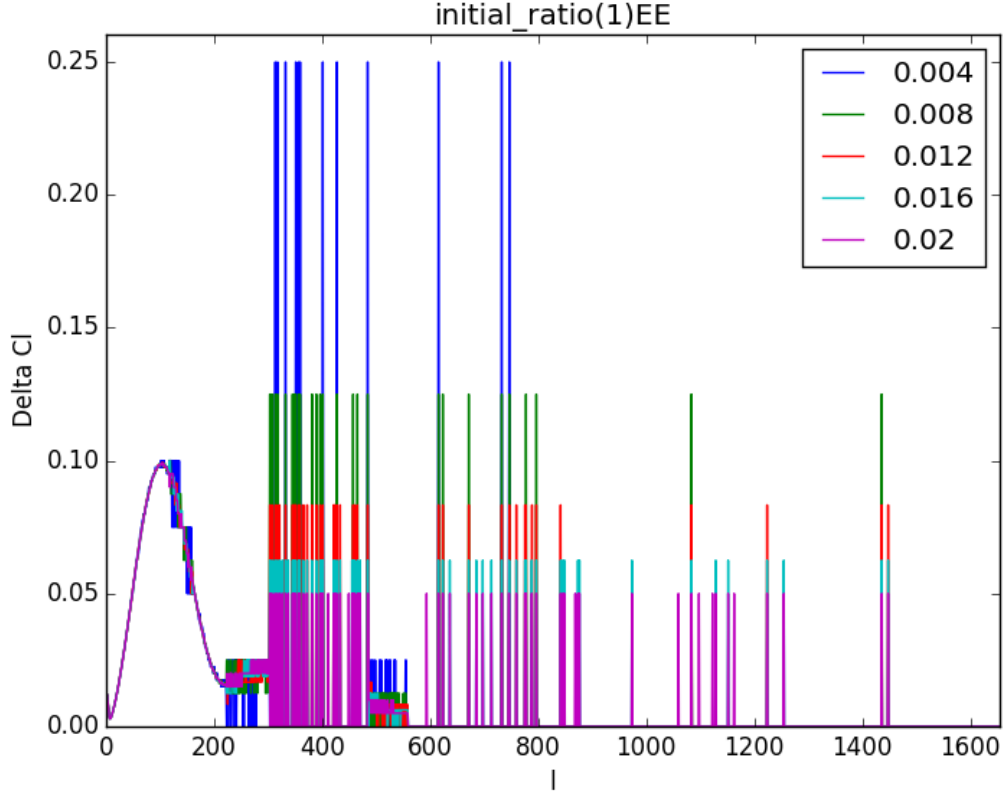
Figure 8: Plot of CMB BB power spectrum difference when r is varied for different step sizes. The plot is convergent and stable for a step size of at least 0.008. After $\ell \approx 220$ numerical effects dominate. These can be ignored due to the low overall contribution of r to the power spectrum.

power spectrum, differentiated with respect to the PMF amplitude: $\frac{\partial C_\ell}{\partial A_{pmf}}$. These templates assume that the PMF strength is $B_{1Mpc} = 2.5nG$ when $A_{pmf} = 1$

3.3   The Covariance Matrix

For the inverse covariance matrix in   15 I used mock stage-3 and stage-4-like covariance matrices. These covariance matrices were calculated as per Tegmark (1997) [Tegmark, 1997] with five experimental parameters: survey area, noise, ℓ_{knee}, beam error and calibration error. The values for these parameters match up with various stage-3 and stage-4 experimental designs.

- Survey area is the area of sky that these experiments will observe given in square degrees. For reference SPT-3G will observe a $2500deg^2$ patch of sky whereas PLANCK observed the whole sky.

- Noise is the background/instrumental(?) noise level of the experiment. This parameter is directly related to the number of bolometers in the experiment.

- ℓ_{knee} is the angular scale where $1/f$ noise starts dominating over the white noise. It is a measure of stability of the experiment and typically larger ℓ_{knee}s equal lower precision on CMB experiments.

- Beam error is the percentage error on the width of the beam. The width of the beam is given by its fwhm.

- Calibration error is the percentage error on the detectors.

In addition to the parameters the covariance matrix also has a prescribed binning. This isn't already implemented so it must be added manually. In order to bin the covariance matrix - and also the templates, I construct a bin matrix. The components of the bin matrix are defined like so:

$$B_{ij} = \begin{cases} (\Delta\ell)^{-1}, & \text{if } j\Delta\ell \leq i \leq (j+1)\Delta\ell \text{ } 0, \\ \text{otherwise} \end{cases} \tag{17}$$

Where $\Delta\ell$ is the length of the bin matrix and $j \leq N_{bin}$, the number of bins. This choice of binning takes the average of the derivative of the power spectrum over each bin.

The bin matrix is then applied to the inverse covariance matrix like so:

$$C_{binned}^{-1} = B^T C^{-1} B \tag{18}$$

Where B is the binning matrix, defined above and C^{-1} is the inverse covariance matrix. The templates are also binned like so:

$$\left(\frac{\partial C_\ell}{\partial p}\right)_{binned} = B\frac{\partial C_\ell}{\partial p} \tag{19}$$

These new binned definitions are then substituted into 15 to construct the Fisher matrix. The output is an $N \times N$ matrix, where N is the number of parameters in the template matrix.

3.4 Conditioning and Forecasting

The range of values along the main diagonal of the Fisher matrix is large, spanning from $\mathcal{O}(10^{24})$ to $\mathcal{O}(10^5)$. The large difference in values makes the Fisher matrix numerically singular under inversion. In order to combat these effects, I use a matrix to bring all the diagonal terms to order unity:

$$M_{ii} = F_{ii}^{(-1/2)} \tag{20}$$

24

This conditioning matrix is applied to the Fisher matrix as per below:

$$F' = M^T F M \tag{21}$$

Once the Fisher matrix is well-conditioned I can then invert it and insert it back into equation 21 to retrieve the covariance matrix for its corresponding mock CMB experiment. The variances for each model parameter are found along the main diagonal and to forecast the experimental uncertainties all I need to do is take the square root of each term.

Since the PMF templates are given in terms of A_{PMF} to forecast for B_{1Mpc} I need to perform a change of variables. Differentiating equation 7 with respect to B_{1Mpc} we have:

$$\frac{\partial A_{pmf}}{\partial B_{1Mpc}} = 4(2.5nG)^{-4} B_{1Mpc}^3 \tag{22}$$

Which can be applied to the Fisher matrix as a transformation in the form of equation 21. For the PMF template we take $B_{1Mpc} = 2.5nG$ when $A_{PMF} = 1$, so the variance of B_{1Mpc}, $\sigma(B_{1Mpc})$ can be expressed as:

$$\sigma(B_{1Mpc}) = 2.5nG \frac{\sigma(A_{PMF})}{4} \tag{23}$$

where $\sigma(A_{PMF})$ is the variance of the PMF amplitude. This relation assumes that the PMF is detected with a field strength of $B_{1Mpc} = 2.5nG$ and all results discussed in section 4 will use this assumption.

4 Forecasts

4.1 Optimising Design Variables

In order to find the best experimental set up and quanitify the improvement from stage-2 to stage-3 or stage-4, I used the mock covariances as described in section 3.3. By varying one experimental variable at a time and holding the rest fixed, I was able to forecast the minimum experimental uncertainty on the PMF strength, $\sigma(B_{1Mpc})$ for each mock experiment and plot the relationship between $\sigma(B_{1Mpc})$ and the experimental variables.
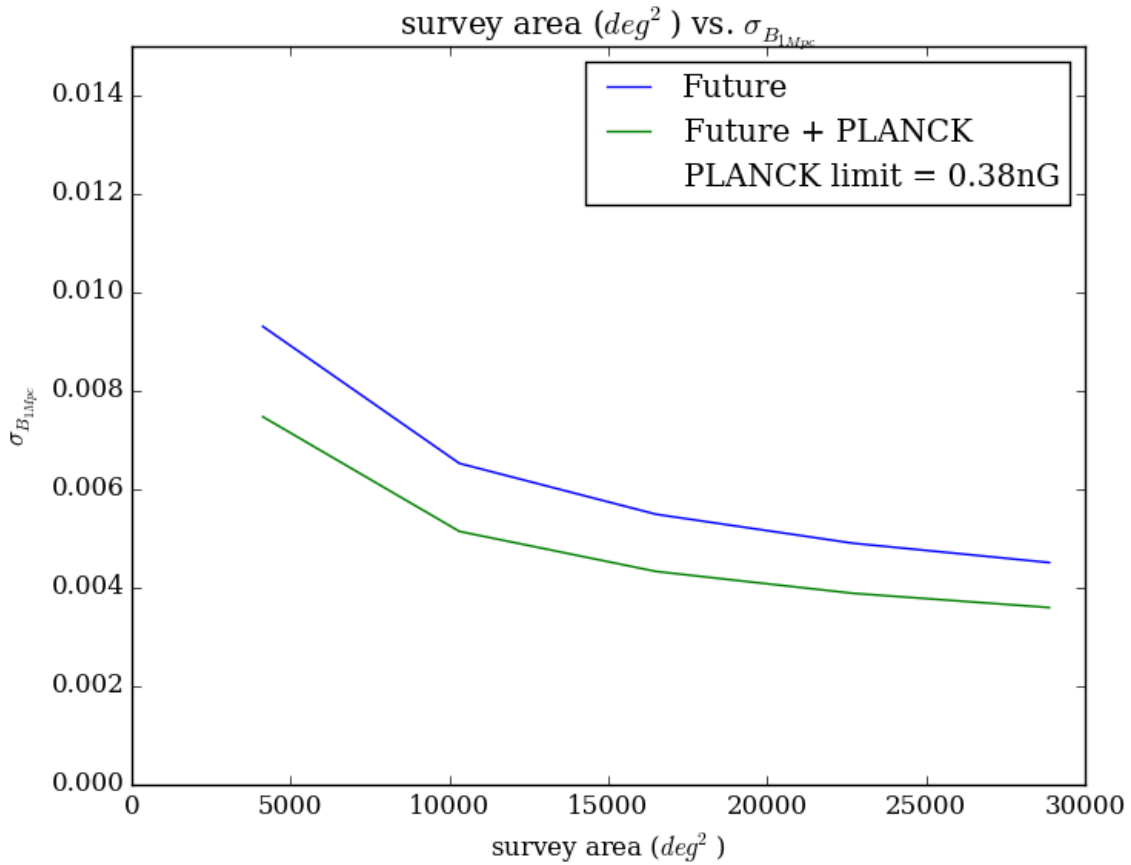

Figure 9: Plot of survey area vs the experimental uncertainty on B_{1Mpc} with all other independent experimental variables held fixed. This plot shows that as the survey area of an experiment increases, the precision on B_{1Mpc} improves, thus the ideal experiment for detecting PMFs will increase the survey area. The blue line shows the precision for Future CMB experiments on their own and the green line shows the same precisions when combined with the PLANCK data set. The data shows a drastic improvement over previous PLANCK constraints of $\sigma(B_{1Mpc}) \geq 0.38nG$.
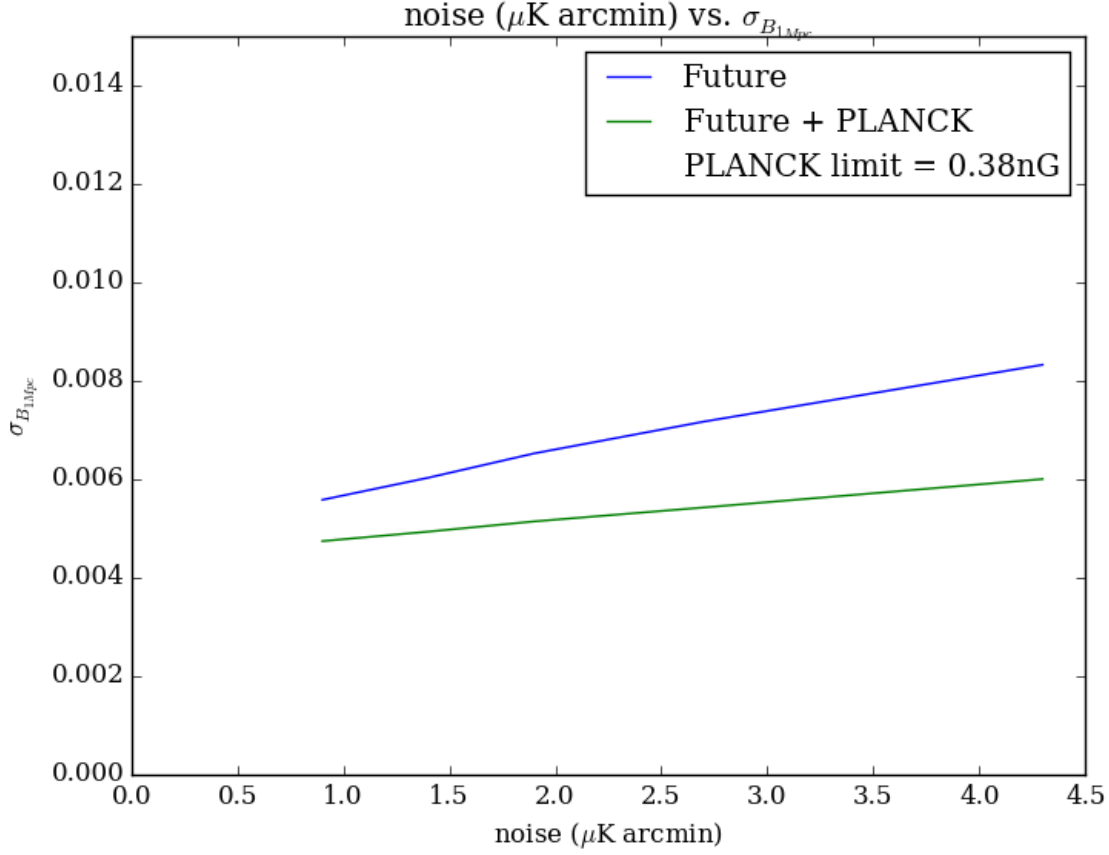
Figure 10: Plot of noise vs the predicted experimental uncertainty on B_{1Mpc}. This plot shows that, as expected, reducing the nosie levels (adding more detectors) improves the constraints on B_{1Mpc}. The blue line shows the predicted limits on $\sigma(B_{1Mpc})$ from future CMB experiments and the green line shows the predicted limits on $\sigma(B_{1Mpc})$ for future experiments combined with current PLANCK constraints. The data shows a significant increase in precision over PLANCK's constraints alone, which were $\sigma(B_{1Mpc}) \geq 0.38nG$.

While varying the experimental design, the fixed values need to be chosen with care. The choice of values will determine how reliable the following forecasts are. The values I chose for the variables are more characteristic to stage-3 experiments than stage-4 ones. The average survey area of a stage-3 experiment is of the order ∼10 000 square degrees (roughly one quarter of the sky). On the other hand, stage-4 experiments are expected to achieve approximately half-sky coverage. Since I chose the stage-3 expected sky coverage, we can expect that the forecasts will underestimate the accuracy gains for stage-4 experiments. On the whole, the values I chose reflect the design specifications of a stage-3 experiment so we would expect the forecasts for stage-4 improvements to be conservative. Table 3 shows the values chosen for a variable when it was held fixed.

The forecasts for the next stages of CMB experiments are promising. Our current best limits from Planck are $\sigma(B_{1Mpc}) \geq 0.38nG$. In comparison, the limits from stage-3 and stage-4-like
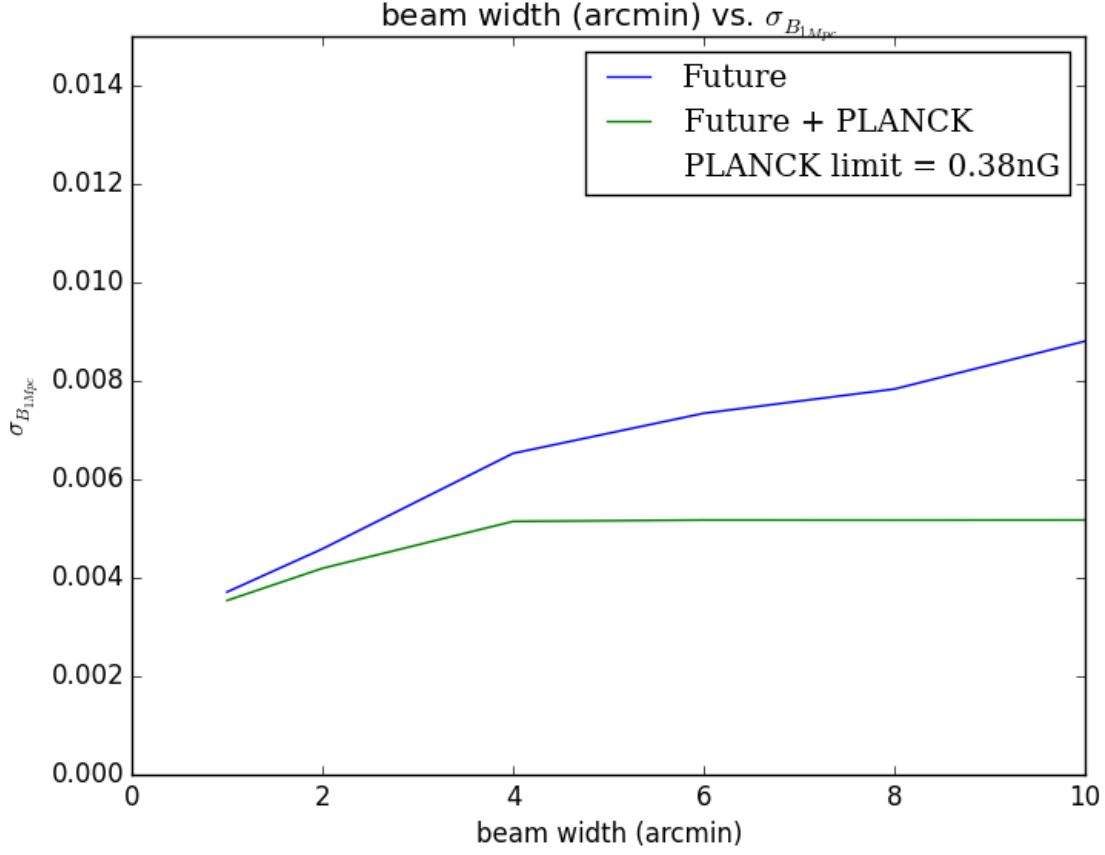
Figure 11: Plot of beam width vs the experimental uncertainty on B_{1Mpc}. This plot shows that reducing the width of the beam reduces the uncertainty on B_{1Mpc}. The blue line shows the best constraints for B_{1Mpc} for future CMB experiments and the green like shows the best constraints for B_{1Mpc} for future CMB experiments plus PLANCK's constraints. Future experiments are expected to improve upon PLANCK's limit of $\sigma(B_{1Mpc}) \geq 0.38nG$ by a wide margin.

covariances fall within the range of ~ 0.01nG to ~ 0.001nG. In the most optimistic cases, measurements will have 100 times more sensitivity to PMFs than current experiments.

The optimal experimental design for detecting PMFs maximises the survey area and minimises the beam width, noise and ℓ_{knee}. The sensitivity is independent of the beam and calibration uncertainties.

As shown in figure 9, $\sigma(B_{1Mpc})$ decreases as the survey area increases. If we combine the mock covariances with PLANCK data our best constraints range from $\sigma(B_{1Mpc}) \geq 0.0075nG$ for a survey area of 4125 deg^2 to $\sigma(B_{1Mpc}) \geq 0.0036nG$ for a survey area of 28877 deg^2, improving by a factor of 2.08. We also see a factor of 1.28 improvement, when the noise decreases from 4.3 μK arcmin to 0.9 μK arcmin, yielding $\sigma(B_{1Mpc}) \geq 0.0060nG$ and $\sigma(B_{1Mpc}) \geq 0.0048nG$ respectively, as seen in figure 10. Decreasing the beam width from 10 arcmin to 1
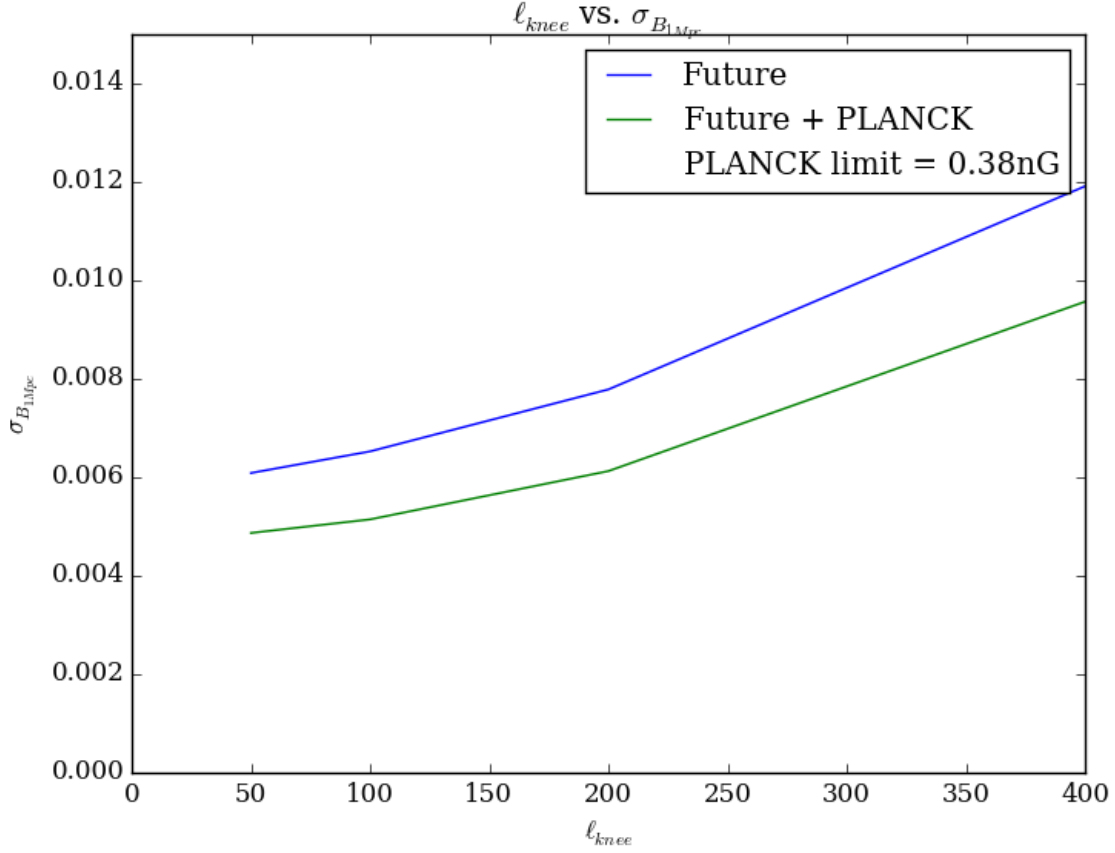
Figure 12: Plot of ℓ_{knee} vs experimental uncertainty on B_{1Mpc} with all other variables held fixed. This plot shows that precision on B_{1Mpc} decreases as ℓ_{knee} increases, so it is best to reduce ℓ_{knee}. The blue line shows the best possible $\sigma(B_{1Mpc})$ for future experiments and the green line shows the best constraints for $\sigma(B_{1Mpc})$ for future experiments combined with prior limits from PLANCK. The data shows vast improvements over PLANCK's previous limit of $\sigma(B_{1Mpc}) \geq 0.38nG$

arcmin improves sensitivity by a factor of 1.46 by reducing the uncertainty from $\sigma(B_{1Mpc}) \geq 0.0052nG$ to $\sigma(B_{1Mpc}) \geq 0.0035nG$ as per figure 11. In figure 12, we see that a lower ℓ_{knee} improves sensitivity. At $\ell_{knee} = 50$, $\sigma(B_{1Mpc}) \geq 0.0049nG$ and in the worst-case scenario, when $\ell_{knee} = 400$, we have $\sigma(B_{1Mpc}) \geq 0.0096nG$ - a factor of 1.96 improvement. In contrast, changes to calibration and beam uncertainty have negligible effects on improving detection limits. For all values of beam and calibration uncertainties the sensitivity to the PMF strength is $\sigma(B_{1Mpc}) \geq 0.0051nG$.

Table 3: Fixed Variables	
Variable	Value
Survey area (deg^2)	10313
Noise (μK arcmin)	1.9
ℓ_{knee}	100
beam width (arcmin)	4.0
calibration error (% error)	0.01
beam uncertainty (% error)	0.05

This table shows the values I chose for each independent variable when they were held fixed. The variables shown are all generous estimates for the range of capabilities the stage-3 experiments will have, but very conservative for stage-4. As a result, the forecasts will underestimate the strengths for the best-case scenario stage-4 experiments.

4.2 Parameter Constraints

Constraining the field strength of PMFs is not the only science goal of future CMB experiments. These experiments are also expected to constrain a wide variety of other model parameters characteristic of extensions to ΛCDM cosmology. In this section I will provide the 1σ confidence contours for B_{1Mpc} and the selection of extended model parameters as described in Section 3.

By inverting Fisher matrices into covariance matrices, one can construct confidence ellipses for pairs of model parameters. The major and minor axes of the ellipse, R_{major} and R_{minor} are given by:

$$R_{major} = \sqrt{\frac{(\sigma_{xx} + \sigma_{yy})}{2} + \sqrt{\frac{(\sigma_{xx} - \sigma_{yy})^2}{4} + \sigma_{xy}^2}} \tag{24}$$

$$R_{minor} = \sqrt{\frac{(\sigma_{xx} + \sigma_{yy})}{2} - \sqrt{\frac{(\sigma_{xx} - \sigma_{yy})^2}{4} + \sigma_{xy}^2}} \tag{25}$$

where σxy are the covariances for the xth and y^{th} model parameter. The angle of orientation of the confidence ellipse, θ is given by:

$$\theta = \frac{1}{2} arctan(\frac{2\sigma_{xy}}{\sigma_{xx} - \sigma_{yy}}) \tag{26}$$

For each contour plot, there are 3 ellipses. The red ellipse represents the present day constraints on the extended model parameters from PLANCK. The blue ellipse represents the forecasted constraints from a typical stage-3 CMB experiment plus PLANCK data. The green ellipse represents the forecasted constraints from a typical stage-4 CMB experiment

plus PLANCK data. For this analysis I set the typical stage-3 experiment as having a survey area of 10313 square degrees, a noise level of 2.7μK arcmin and $\ell_{knee} = 100$. The typical stage-4 experiment improves on these variables with approximately two times the survey area, 22689 square degrees, half the noise, at 1.3μK arcmin and $\ell_{knee} = 50$. Table 4 shows the full set of 'typical' values I chose for the experimental variables of stage-3 and stage-4 experiments.

Table 4: Mock Stage-3 and Stage-4 Variables

Variable	Stage-3	Stage-4
Survey area (deg^2)	10313	22689
Noise (μK arcmin)	2.7	1.3
ℓ_{knee}	100	50
beam width (arcmin)	4.0	4.0
calibration error (% error)	0.01	0.01
beam uncertainty (% error)	0.05	0.05

This table shows the values for each variable for both the mock covariance matrices used to construct the confidence ellipses. We see that from stage-3 to stage-4, the survey area will more than double from 10313 square degrees to 22689 square degrees, the noise will halve from 2.7μK arcmin to 1.3μK arcmin as will ℓ_{knee} - from 100 to 50. On the other hand, beam width will remains fixed at 4.0 arcmin and both beam and calibration errors stay at 0.05% and 0.01% respectively.

As shown in figure 13, stage-3 and stage-4 experiments make major improvements on B_{1Mpc} and moderate improvements over n_{run} from PLANCK results. The gains in precision in n_{run} are significant from stage-3 to stage-4 in contrast to the gains in B_{1Mpc}. This relationship between $\sigma B_{1Mpc})$ and $\sigma n_{run})$ indicates that future CMB experiments will be effective for providing constraints on n_{run}. Additionally, There is a very weak degeneracy between the two parameters according to the PLANCK contour which seems to be broken by the contours from stage-3 and stage-4.

Figure 14 shows that stage-3 and stage-4 experiments make moderate improvements on constraining N_{eff} from current PLANCK results. The graph also shows that within PLANCK data there exists a degeneracy between the B_{1Mpc} and the effective number of neutrinos. Stage-3 and stage-4 appear to break this degeneracy. Given the magnitude of the decrease in the size of the contours from PLANCK to stage-3 to stage-4, there is something to gain from using data from future CMB experiments to constrain N_{eff}.

Finally, figure 15 shows a drastic improvement on the constraints of r from PLANCK to the next generations. This is to be expected since detecting primordial gravity waves from inflation is one of the primary science goals of ground-based CMB polarisation experiments. Data from stage-3 and stage-4 do not break the degeneracy that existed in PLANCK between B_{1Mpc} and r however. As a result, other methods for constraining the values of these parameters will be needed.
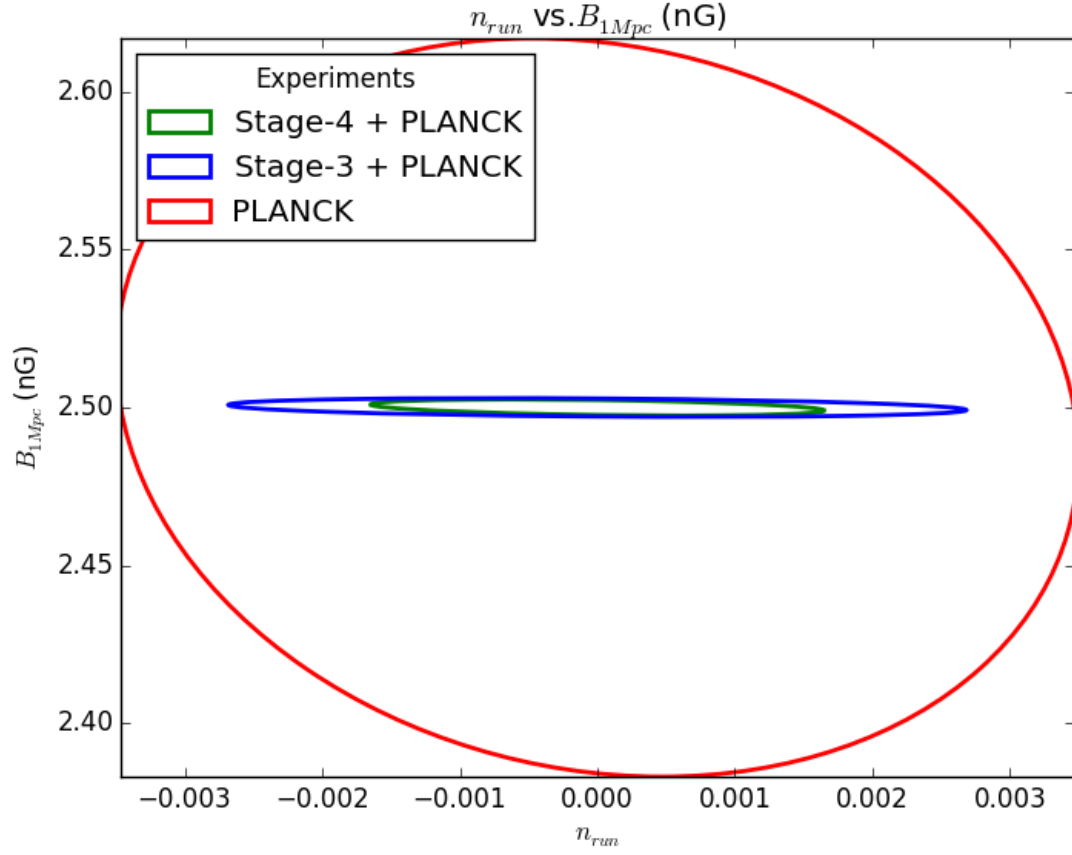
31

Figure 13: This is a plot of the 1σ confidence contours for n_{run} vs. B_{1Mpc}. The red line shows the confidence contour for previous PLANCK data. The blue contour shows the confidence contour for stage-3 CMB experiments plus PLANCK data. The green contour shows the confidence contour for stage-4 CMB experiments plus PLANCK data. The plot shows a large forecasted improvement on the stage-3 and stage-4 precisions on B_{1Mpc} over the previous PLANCK constraints. Improvements on n_{run} increase from PLANCK to stage-3 and again from stage-3 to stage-4.
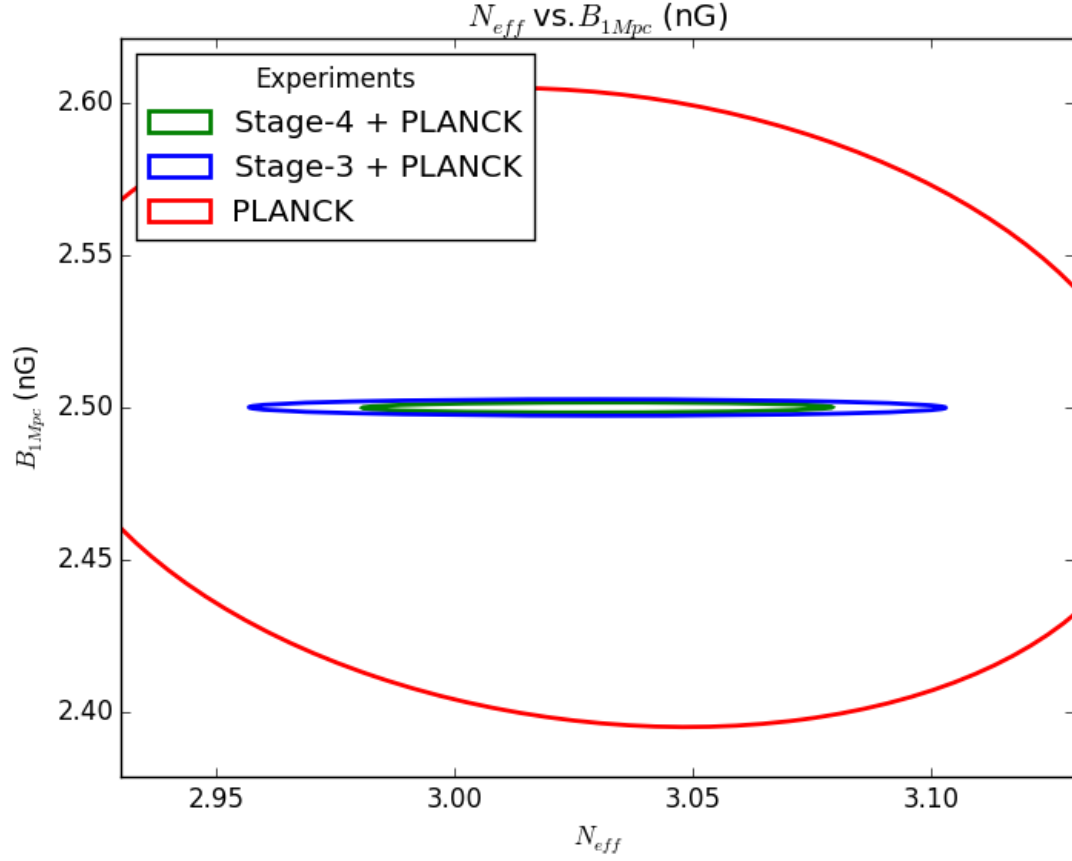
Figure 14: This is a plot of the 1σ confidence contours for N_{eff} vs. B_{1Mpc}. The red line shows the confidence contour for previous PLANCK data. The blue contour shows the confidence contour for stage-3 CMB experiments plus PLANCK data. The green contour shows the confidence contour for stage-4 CMB experiments plus PLANCK data. The plot shows moderate improvements on $\sigma(B_{1Mpc})$, with stage-4 experiments possessing the tightest constraints, as expected. N_{eff} sees a large forecasted improvement on its constraints from previous PLANCK data.
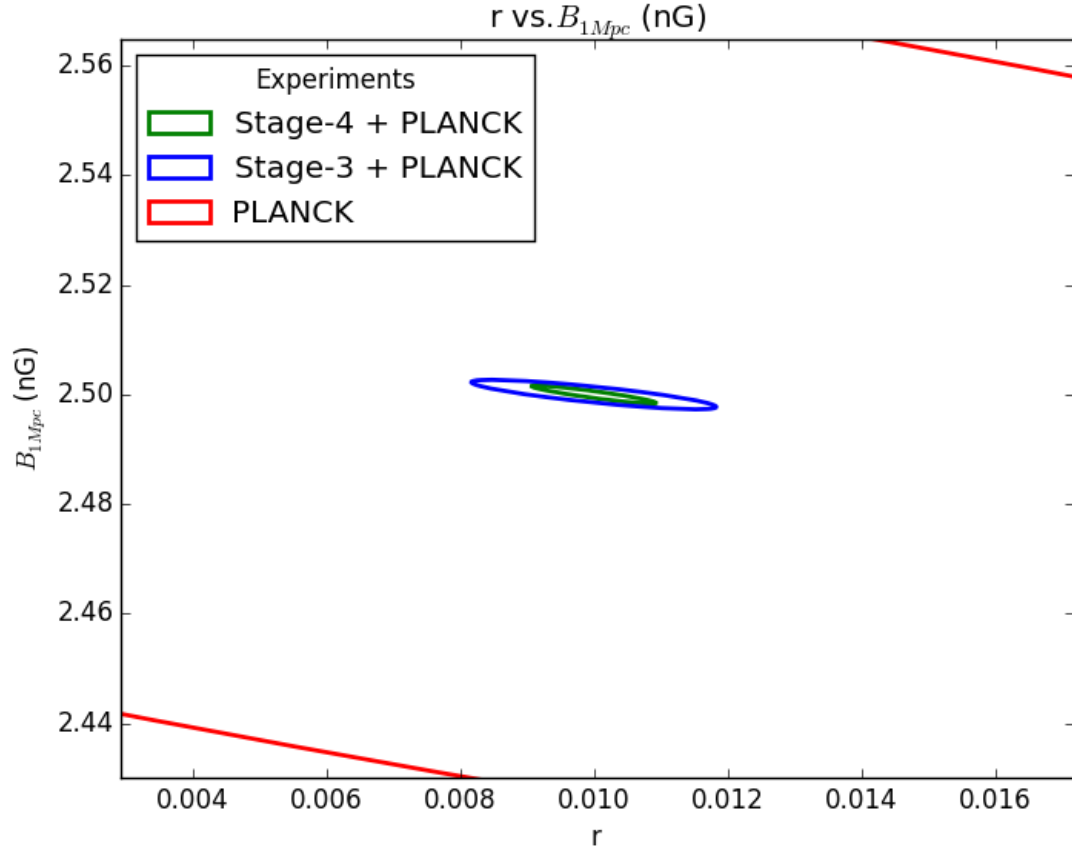
Figure 15: This is a plot of the 1σ contours for r vs. B_{1Mpc}. The red line shows the confidence contour for previous PLANCK data. The blue contour shows the confidence contour for stage-3 CMB experiments plus PLANCK data. The green contour shows the confidence contour for stage-4 CMB experiments plus PLANCK data. There is a large forecasted improvement in both the constraints on B_{1Mpc} and r over previous PLANCK data, however neither stage-3 or stage-4 are expected to break the degeneracy between B_{1Mpc} and r.

5 Discussion and Future Work

5.1 Discussion

PMFs are a prime candidate for a weak seed magnetic field that, through amplification by galactic dynamos could explain the origins of the weak large-scale magnetic fields that thread the cosmos. Indirect detection of PMFs through measuring the B-mode polarisation power spectrum in the CMB holds promise for testing the model. Previous work from POLARBEAR has given the upper limit on the primordial magnetic field strength smoothed over 1 megaparsec as $B_{1Mpc} \leq 3.9nG$. In late 2016 the next generation of CMB experiments, known as stage-3 will begin operation followed by stage-4 in the early 2020s. Though not the main science goal of these experiments, stage-3 and stage-4 may be able to detect the faint traces of PMFs within the CMB. In the interest of time and money, it is useful to know beforehand just how sensitive these experiments will be to PMF signals.

Using simulated CMB power spectra with an effective 2.5nG PMF and mock covariance matrices for future CMB experiments, I was able to forecast the limits on $\sigma(B_{1Mpc})$ for stage-3 and stage-4 CMB experiments. With these forecasts I was able to test the impact on $\sigma(B_{1Mpc})$ from varying the experimental design variables, survey area, noise, beam width, ℓ_{knee}, beam uncertainty and calibration error. I found that the optimal experimental design for detecting a PMF with a field strength of 2.5nG maximises the scan area, minimises the noise, ℓ_{knee} and the beam width and is independent of beam uncertainty and calibration error. The lowest variance I found with this method was $\sigma(B_{1Mpc}) \geq 0.0036nG$ for a survey area of 28877 square degrees with all other experimental variables fixed. This result reflects the best case scenario for stage-4 CMB epxeriments. These results all drastically improve - by up to a factor of 100 - upon current-day constraints taken from PLANCK, which currently has $\sigma(B_{1Mpc}) \geq 0.38nG$.

In addition to finding the best experimental design variables I also plotted the 1σ contours for current PLANCK data, stage-3 expected and stage-4 expected constraints on B_{1Mpc}, tensor-to-scalar ratio r, running of the scalar spectral index n_{run} and the effective number of neutrinos N_{eff}. As expected, stage-3 and stage-4 experiments improve constraints for all these parameters. We see that future CMB experiments offer moderate improvements on n_{run} and major improvements on N_{eff} and r from current PLANCK results. There are no clear degeneracies between n_{run} and B_{1Mpc} nor N_{eff} and B_{1Mpc}, however there is a degeneracy between r and B_{1Mpc}, which is not broken by stage-3 or stage-4.

5.2   Future Work

There are still many avenues for further research in this area including repeating the analysis for other PMF parameters, tightening the constraints with extra data and adding more CDM extension parameters to the Fisher matrix.

In addition to forecasting $\sigma(B_{1Mpc})$, we could also forecast for other PMF parameters. Two options with lots of promise are n_{PMF}, the spectral index for the PMF power spectrum and β, the PMF era. n_{PMF} is a direct probe of the generation mechanism for PMFs. By tightening the confidence intervals on n_{PMF} we can more confidently rule out proposed generation mechanisms. β on the other hand, tell us the age of the Universe when PMFs first formed. If we can measure these two parameters we would have a very clear picture of how PMFs fit into the cosmos. To do this though, we must first design an experiment that can detect these parameters, hence it is essential that we repeat the analysis done here to find the optimal experimental designs for measuring n_{PMF} and β.

Another direction we could take is to further improve upon the forecasted constraints here by using covariances from other experiments, inverting them into a Fisher matrix and adding them to our own. By doing this we may not only find that $\sigma(B_{1Mpc})$ decreases significantly but also break degeneracies between PMF parameters and the extensions to ΛCDM. In a similar vein it may prove useful to add further extensions to ΛCDM model parameters to find out how a PMF analysis would constrain the wider parameter space.

Finally, in this analysis we assumed that future experiments would detect a PMF with a field strength of 2.5nG. This is not necessarily the case, POLARBEAR has constrained the field strength to $B_{1Mpc} \leq 3.9nG$, so all values in this domain are plausible. In the future we could carry out an analysis for a range of different magnetic field strengths.

References

[Abazajian et al., 2015] Abazajian, K. N. et al. (2015). Neutrino Physics from the Cosmic Microwave Background and Large Scale Structure. *Astropart. Phys.*, 63:66–80.

[Adam et al., 2016] Adam, R. et al. (2016). Planck 2015 results. VIII. High Frequency Instrument data processing: Calibration and maps. *Astron. Astrophys.*, 594:A8.

[Ade et al., 2015a] Ade, P. A. R. et al. (2015a). Planck 2015 results. XIII. Cosmological parameters.

[Ade et al., 2015b] Ade, P. A. R. et al. (2015b). Planck 2015 results. XIX. Constraints on primordial magnetic fields.

[Ade et al., 2015c] Ade, P. A. R. et al. (2015c). POLARBEAR Constraints on Cosmic Birefringence and Primordial Magnetic Fields. *Phys. Rev.*, D92:123509.

[Beck et al.,] Beck, R., Brandenburg, A., Moss, D., Shukurov, A., and Sokoloff, D.

[Benson et al., 2014] Benson, B. A. et al. (2014). SPT-3G: A Next-Generation Cosmic Microwave Background Polarization Experiment on the South Pole Telescope. *Proc. SPIE Int. Soc. Opt. Eng.*, 9153:91531P.

[Buczilowski and Beck, 1991] Buczilowski, U. R. and Beck, R. (1991). A multifrequency radio continuum survey of M33. III - The magnetic field. , 241:47–56.

[Giovannini, 2004] Giovannini, M. (2004). The Magnetized universe. *Int. J. Mod. Phys.*, D13:391–502.

[Gluscevic et al., 2009] Gluscevic, V., Kamionkowski, M., and Cooray, A. (2009). Derotation of the cosmic microwave background polarization: Full-sky formalism. *Phys. Rev. D*, 80:023510.

[Henderson et al., 2016] Henderson, S. W. et al. (2016). Advanced ACTPol Cryogenic Detector Arrays and Readout. *J. Low. Temp. Phys.*, 184(3-4):772–779.

[Hu and White, 1997] Hu, W. and White, M. J. (1997). A CMB polarization primer. *New Astron.*, 2:323.

[Kawasaki and Kusakabe, 2012] Kawasaki, M. and Kusakabe, M. (2012). Updated constraint on a primordial magnetic field during big bang nucleosynthesis and a formulation of field effects. *Phys. Rev. D*, 86:063003.

[Krauss et al., 2010] Krauss, L., Dodelson, S., and Meyer, S. (2010). Primordial gravitational waves and cosmology. *Science*, 328(5981):989–992.

[Lamarre et al., 2003] Lamarre, J.-M. et al. (2003). The planck high frequency instrument, a 3rd generation cmb experiment, and a full sky submillimeter survey. *New Astron. Rev.*, 47:1017.

[Robishaw et al., 2008] Robishaw, T., Quataert, E., and Heiles, C. (2008). Extragalactic Zeeman Detections in OH Megamasers. *Astrophys. J.*, 680:981.

[Suzuki et al., 2016] Suzuki, A. et al. (2016). The POLARBEAR-2 and the Simons Array Experiment. *J. Low. Temp. Phys.*, 184(3-4):805–810.

[Tegmark, 1997] Tegmark, M. (1997). CMB mapping experiments: A Designer's guide. *Phys. Rev.*, D56:4514–4529.

[Turner and Widrow, 1988] Turner, M. S. and Widrow, L. M. (1988). Inflation-produced, large-scale magnetic fields. *Phys. Rev. D*, 37:2743–2754.

[Widrow, 2002] Widrow, L. M. (2002). Origin of galactic and extragalactic magnetic fields. *Rev. Mod. Phys.*, 74:775–823.